Photonics-assisted Technologies for Extreme Broadband 5G Wireless Communications

Xinying Li, member, IEEE, member, OSA, Jianjun Yu, Senior Member, IEEE, Fellow, OSA, and Gee-Kung Chang, Fellow, IEEE, Fellow, OSA

(Invited Paper)

***Abstract*—We summarize the enabling technologies for photonics-assisted broadband millimeter-wave (mm-wave) communication, which is a promising candidate for the enhanced mobile broadband (eMBB) communications, one of the three main typical application scenarios of 5G wireless networks. These enabling technologies, mainly focusing on the improvement of the system structure, include broadband mm-wave signal generation with simple and cost-effective schemes, multiple-input multiple-output (MIMO) architecture with polarization-multiplexing optical mm-wave signal, advanced multi-level modulation, optical or electrical multi-carrier modulation, antenna polarization multiplexing and the employment of the high-gain mm-wave antenna, multi-band multiplexing, and broadband mm-wave signal detection. We also review the advanced digital signal processing (DSP) for heterodyne coherent detection, which can be applied into the photonics-assisted mm-wave communication systems, to further enhance the system performance for a given system structure and certain available devices. Based on these enabling technologies and advanced DSP, we have realized over 1-Tb/s wireless signal transmission at D-band and over 2.5-km wireless transmission with a bit rate up to 54Gb/s at W-band. Our work verifies the photonics-assisted broadband mm-wave communication can meet the high-data-rate demand of eMBB.**

***Index Terms*—5G wireless networks, enhanced mobile broadband communications, photonics-assisted millimeter-wave generation, digital signal processing, millimeter-wave communication, multi-level modulation, polarization multiplexing, antenna polarization multiplexing, heterodyne coherent detection, fiber wireless integration.**

I. Introduction

Enhanced mobile broadband (eMBB) communications is one of the grand challenges of 5G and beyond wireless networks that require more bandwidth at higher frequencies [1-4]. The application scenarios of eMBB will include ubiquitous virtual reality/augmented reality (VR/AR), artificial intelligence, 4k/8k high-definition video, and so on, which will bring in an explosive data traffic demanding higher data rate. Therefore, it is interesting to investigate how to realize mobile data transmission at a data rate as high as possible. Millimeter-wave (mm-wave) band (30GHz-300GHz) is one of the promising candidates for 5G, since its huge bandwidth can accommodate higher data rate [5-8].

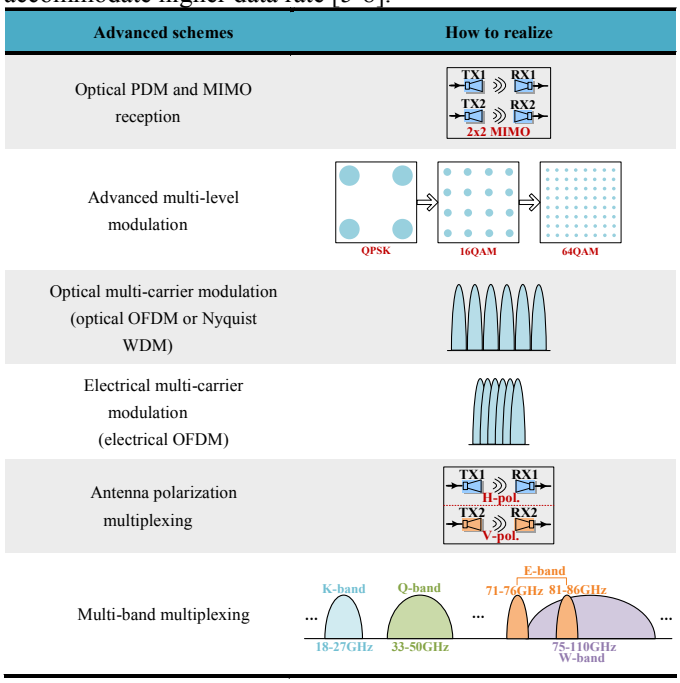

Fig. 1. Representative enabling technologies to realize photonics-assisted mm-wave communication with ultra-wide bandwidth.

Since 2010, the high-speed optical transceiver with 100Gb/s per channel based on coherent detection has been widely deployed in the practical optical systems and networks [9]. These systems and networks use quadrature-amplitude-modulation (QAM) modulation at the transmitter side and coherent detection at the receiver side to realize high-spectral-efficiency and long-distance signal transmission. Advanced digital signal processing (DSP) is also employed to solve the problems of fiber dispersion, signal polarization separation,

Manuscript received xx, 2018. This work was partially supported by the NNSF of China (61527801, 61675048, 61720106015, 61835002, and 61805043). (Corresponding author: Gee-Kung Chang.)

X. Li is with Georgia Institute of Technology, Atlanta 30332, GA, and also with Shanghai Institute for Advanced Communication and Data Science, Key Laboratory for Information Science of Electromagnetic Waves (MoE), State Key Laboratory of ASIC and System, Fudan University, Shanghai 200433, China (e-mail: xinying.li@ece.gatech.edu).

J. Yu is with Shanghai Institute for Advanced Communication and Data Science, Key Laboratory for Information Science of Electromagnetic Waves (MoE), Fudan University, Shanghai 200433, China (e-mail: jianjun@fudan.edu.cn).

G.-K. Chang is with Georgia Institute of Technology, Atlanta 30332, GA (e-mail: geekung.chang@ece.gatech.edu).

frequency offset and phase noise, and so on. These advanced DSP is quite mature and widely employed in the practical devices. Moreover, the photonic devices, such as external optical modulator, have very wide bandwidth, and devices with >70-GHz bandwidth are already available [10]. Compared to the electrical in-phase/quadrature (I/Q) mixer with limited bandwidth, the optical I/Q modulator can get the bandwidth over 40GHz [10]. As a result, it is a natural choice to use photonics-assisted technologies to solve the bandwidth limitation of electrical mm-wave communication.

In this paper, we will summarize a series of different enabling technologies to realize photonics-assisted mm-wave communication with ultra-wide bandwidth to meet the eMBB challenge in 5G. These enabling technologies mainly focus on the improvement of the system structure and will be presented in Section II. They include broadband mm-wave signal generation with simple and cost-effective schemes, multiple-input multiple-output (MIMO) architecture with polarization-multiplexing optical mm-wave signal, advanced multi-level modulation, optical or electrical multi-carrier modulation, antenna polarization multiplexing and the employment of the high-gain mm-wave antenna, multi-band multiplexing, and broadband mm-wave signal detection. Fig. 1 shows the schematic diagram of several representative enabling technologies mentioned above. In Section III, we will discuss a series of advanced DSP for heterodyne coherent detection, which can be applied into the photonics-assisted mm-wave communication systems, to further enhance the system performance for a given system structure and certain available devices. Based on these enabling technologies and advanced DSP, we have realized wireless transmission at D-band with a record capacity of >1Tb/s of and 54-Gb/s signal wireless transmission over 2.5-km distance at W-band, which will be presented in Section IV. Section IV also gives a theoretical analysis on the transmission performance of the wireless mm-wave links. Finally, Section V summarizes the whole paper.

II. Enabling Technologies for Broadband Mm-Wave Communication

In this Section, mainly focusing on the system structure improvement, we will introduce a series of advanced enabling technologies, including broadband mm-wave signal generation with simple and cost-effective schemes, MIMO architecture with polarization-multiplexing optical mm-wave signal, advanced multi-level modulation, optical or electrical multi-carrier modulation, antenna polarization multiplexing and the employment of the high-gain mm-wave antenna, multi-band multiplexing, and broadband mm-wave signal detection. The employment of these enabling technologies can reduce the signal baud rate and the required bandwidth for optical and electrical devices, and therefore promote the realization of photonics-assisted broadband mm-wave communication.

A. Broadband Mm-Wave Signal Generation with Simple and Cost-Effective Schemes

Photonic mm-wave signal generation with simple and cost-effective schemes is one of the key technologies for broadband mm-wave communication. The simple and common method for photonic mm-wave generation is the heterodyne beating of two continuous-wavelength (CW) lightwaves generated from two free-running lasers [11]. This method can generate the mm-wave signal with a tunable carrier frequency and a relatively high signal-to-noise ratio (SNR). However, the generated mm-wave signal by this method has an unstable carrier frequency, which may not be suitable for 5G since 5G services need a very stable network environment [1, 2]. We can also use the optical multi-carrier source to generate the mm-wave signal [12-15]. In this method, we need to use an optical filter to select two generated optical subcarriers with a certain frequency spacing from the optical multi-carrier source. Then we modulate one selected subcarrier while keeping the other unmodulated, before they are heterodyne beat in a photodiode (PD). This method can make full use of low-bandwidth optoelectronic devices to generate broadband mm-wave signal but at a cost of relatively complicated structure. Moreover, the generated mm-wave signal by this method has a relatively small SNR since the power of each generated optical subcarrier is reduced relative to the original optical carrier. Recently, the optical mm-wave generation based on a single optical intensity or phase modulator and photonic frequency multiplication has been proved to be a good scheme, because it can generate stable optical mm-wave signal with a simple structure and the reduced bandwidth requirements for optical and electrical devices [16-25]. However, this method needs transmitter-based precoding for vector mm-wave signal generation [20-25], since the two optical subcarriers used for heterodyne beating both carry signals, which will increase the computational complexity.

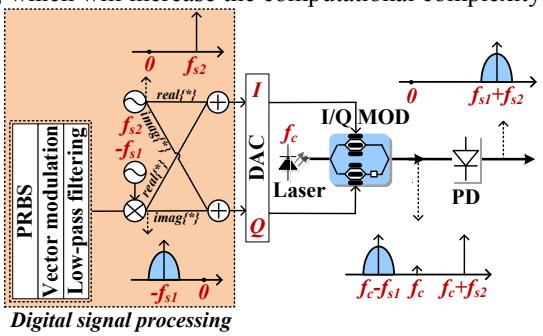

Fig. 2. Principle of photonic vector mm-wave signal generation by only one external modulator without optical filter. DAC: digital-to-analog converter, I/Q MOD: I/Q modulator, PD: photodiode.

In Ref. 26, we proposed a scheme to generate photonic vector mm-wave signal adopting optical asymmetric single-sideband (ASSB) modulation through the use of an I/Q modulator. This scheme is very simple and cost effective. Fig. 2 shows the principle of our proposed scheme. For single-sideband (SSB) signal generation, we can use a complex sinusoidal radio-frequency (RF) source with one-sided spectrum, which can be generated if we remove the positive or negative spectrum of a real sinusoidal RF source by Hilbert-transform phasing method [27-30]. During the transmitter DSP, the baseband vector signal is linearly up-converted to a lower-sideband (LSB) vector signal located at carrier frequency $-f_{s1}$ after mixing with a complex sinusoidal RF source at negative frequency $-f_{s1}$. The baseband vector signal can adopt quadrature-phase-shift-keying (QPSK), 8-ary quadrature amplitude modulation (8QAM), 16QAM, 64QAM and so on. Then the real and imaginary parts of the LSB vector signal are

added with the real and imaginary parts of a complex sinusoidal RF source at positive frequency f_{s2}, respectively. After that, we send them into the I and Q input ports of a digital-to-analog converter (DAC). We can set f_{s1} and f_{s2} to be equal or unequal. The electrical I and Q outputs of the DAC are employed to drive the I and Q ports of an I/Q external modulator, respectively. A SSB electrical signal can be linearly converted to a SSB optical signal when its real and imaginary parts are used to drive an I/Q modulator [27-30]. Therefore, after the I/Q modulator, we can generate a vector-modulated optical LSB at frequency f_c-f_{s1} and an unmodulated optical USB at frequency f_c+f_{s2}. Then, we use a single-ended PD to convert the generated optical mm-wave signal into an electrical vector mm-wave signal at frequency f_{s1}+f_{s2}. This optical mm-wave signal can be transmitted over a long-distance fiber since in this case only one sideband carries signal [31].

B. MIMO Architecture with Polarization-Multiplexing Optical Mm-Wave Signal

Fig. 3 shows the schematic diagram of the polarization-multiplexing mm-wave signal generation, wireless transmission, and heterodyne detection based on a MIMO architecture [32]. It includes polarization-multiplexing optical baseband signal generation by an optical baseband transmitter, polarization-multiplexing electrical mm-wave signal generation by an optical heterodyne up-converter, wireless transmission by a 2×2 MIMO link, and analog down conversion and offline DSP demodulation by a wireless mm-wave receiver.

First, we need to generate a polarization-multiplexing optical mm-wave signal. The optical mm-wave signal can be generated by the schemes mentioned in Section IIA. For polarization-multiplexing optical mm-wave signal, we can use two optical mm-wave signals with orthogonal polarization but the same optical frequency, which can be generated from the same CW lightwave before combined by an optical coupler (OC) [32]. We can also use a polarization-multiplexing I/Q modulator to generate two optical mm-wave signals with orthogonal polarization [33]. Fiber dispersion will affect the transmission distance of the optical mm-wave signals. There are some schemes to overcome fiber dispersion, and SSB is one of the good schemes [11, 31].

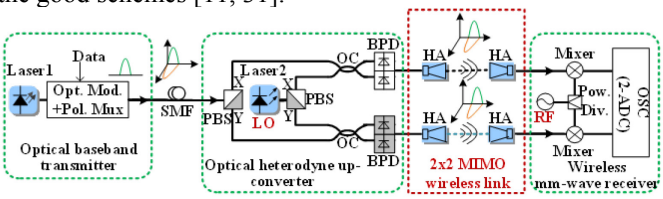

Fig. 3. Schematic diagram for polarization-multiplexing mm-wave signal generation, wireless transmission, and heterodyne detection based on a MIMO architecture. Opt. Mod.: optical modulator, Pol. Mux: polarization multiplexer, SMF: single-mode fiber, PBS: polarization beam splitter, LO: local oscillator, OC: optical coupler, BPD: balanced photodiode, HA: horn antenna, Pow. Div.: power divider.

For the generation of the polarization-multiplexing electrical mm-wave signal, we can employ individual optical components including two OCs and two optical polarization beam splitters (PBSs), or an integrated polarization-diversity phase-diversity 90-degree optical hybrid, to separate polarization-multiplexing optical signals before they are detected by two high-speed PDs [34-48]. Here, compared to two single-ended PDs, the employment of two balanced PDs will obtain a better performance because they can cancel the noise and improve the input power of the optical signals [49]. Two electrical mm-wave signals are generated after the two high-speed PDs, and they can be considered as a polarization-multiplexing electrical mm-wave signal. Note that currently the PD can have a bandwidth over 170GHz [46], and therefore in this case, up to 170-GHz mm-wave carrier can be generated. The wireless transmission of the polarization-multiplexing electrical mm-wave signal is realized by a 2×2 MIMO link including two transmitter antennas and two receiver antennas [37]. The antennas have different types, which will be discussed in Section IIF. Currently the commercial analog-to-digital converter (ADC) or real-time oscilloscope can have a bandwidth up to 100GHz although it is very expensive. If we use the lower-cost one with insufficient bandwidth, we will first need to perform the analog down conversion of the mm-wave signals. We can use a balanced mixer driven by an electrical local oscillator (LO) to down-convert the mm-wave signals to lower-frequency intermediate-frequency (IF) signals before a real-time oscilloscope with two ports detects them. The recorded data in the real-time oscilloscope will be analyzed by advanced DSP [49, 50].

Here, we use $(E_{in,x}, E_{in,y})^T$ to denote the original X- and Y-polarization components of the optical baseband signal generated by the optical baseband transmitter, the received optical signal $(E_{out1,x}, E_{out1,y})^T$ by the optical heterodyne up-converter can be expressed as

$$\begin{pmatrix} E_{out1,x} \\ E_{out1,y} \end{pmatrix} = \begin{pmatrix} J_{xx} & J_{xy} \\ J_{yx} & J_{yy} \end{pmatrix} \begin{pmatrix} E_{in,x} \\ E_{in,y} \end{pmatrix} = J \begin{pmatrix} E_{in,x} \\ E_{in,y} \end{pmatrix}. \quad (1)$$

Where J is a 2×2 Jones matrix and denotes the transfer function for the fiber transmission from the optical baseband transmitter to the optical heterodyne up-converter. J_{xx} and J_{yy} denote the crosstalk between the original X- and Y-polarization components caused by the fiber transmission.

Next, the received wireless mm-wave signal by the wireless mm-wave receiver can be expressed as

$$\begin{pmatrix} E_{out2,x} \\ E_{out2,y} \end{pmatrix} = \begin{pmatrix} W_{xx} & W_{xy} \\ W_{yx} & W_{yy} \end{pmatrix} \begin{pmatrix} E_{out1,x} \\ E_{out1,y} \end{pmatrix} \cos wt = W \begin{pmatrix} E_{out1,x} \\ E_{out1,y} \end{pmatrix} \cos wt. \quad (2)$$

Where W is a 2×2 gain matrix and denotes the transfer function for the 2×2 MIMO wireless transmission from the optical heterodyne up-converter to the wireless mm-wave receiver. W_{xy} and W_{yx} denote the crosstalk between the original X- and Y-polarization components caused by the wireless transmission, which means each receiver antenna can simultaneously detect the wireless signals from two transmitter antennas. When two pairs of transmitter and receiver antennas have a high directionality and each receiver antenna can only detect the wireless signal from the corresponding transmitter antenna, the values of W_{xy} and W_{yx} are approximately zero. w is mm-wave carrier frequency. By combining Eq. 1 and Eq. 2, we can get

$$\begin{pmatrix} E_{out2,x} \\ E_{out2,y} \end{pmatrix} = WJ \begin{pmatrix} E_{in,x} \\ E_{in,y} \end{pmatrix} \cos(wt) = H \begin{pmatrix} E_{in,x} \\ E_{in,y} \end{pmatrix} \cos(wt). \quad (3)$$

Where the total transfer function H for the fiber-wireless link, as the product of two 2×2 matrixes, is still a 2×2 matrix. Therefore, the classic constant-modulus-algorithm (CMA) equalization with a 2×2 butterfly structure can be used at the

receiver to simultaneously realize signal polarization demultiplexing and wireless crosstalk suppression [51, 52].

C. Advanced Multi-Level Modulation

Long wireless transmission distance and high spectral efficiency cannot be met at the same time. We can get a high spectral efficiency using high-order QAM, because in this case each symbol can carry more bits. However, the high-order QAM mm-wave signal needs more input power or SNR at the receiver side because it has a smaller Euclidean distance between adjacent constellation points [53]. If we need a longer wireless transmission, we should use low-order QAM, such as QPSK [54] or 8QAM [55]. We have demonstrated 8QAM signal transmission with a bit rate of 54Gb/s over 2.5-km wireless distance at W-band [55]. We have demonstrated high-order QAM, such as 16QAM [39, 55] and 64QAM [47, 48], mm-wave transmission with a limited wireless transmission distance of 1~2 meters. Nonlinear effects of optical and electrical devices severely limit the performance of high-order QAM, and advanced DSP is required to reduce these nonlinear effects [56-58].

D. Optical or Electrical Multi-Carrier Modulation

We can reduce the baud rate of an optical or electrical signal if we use multi-carrier modulation. In Ref. 51, we have demonstrated three-channel wireless transmission by using optical multi-carrier generation. Because the baud rate is relatively small after employing optical multi-carrier modulation, the demonstrated system has a better tolerance to the fading effect in transmission fiber. We delivered the three-channel 3×40-Gb/s mm-wave signal over 80-km fiber and 2-m 2×2 MIMO wireless link at 92-GHz W-band. The three-channel 3×40-Gb/s optical PDM-QPSK signal with 12.5-GHz channel spacing was up-converted to 92-GHz wireless carrier by optical polarization-diversity heterodyne beating [51].

Orthogonal-frequency-division-multiplexing (OFDM) modulation is one kind of electrical multi-carrier modulation and it is widely used in the wireless networks [27]. OFDM used in the optical networks can be used to overcome fiber dispersion and polarization mode dispersion (PMD) as well as to provide high spectral efficiency [59-64]. In Ref. 59, we experimentally demonstrated 30.67-Gb/s OFDM signal transmission over 40-km standard single-mode fiber (SSMF) and 5-m wireless link at 100GHz, adopting MIMO and heterodyne coherent detection. The bit-error ratio (BER) after both wireline and wireless transmission is smaller than 3.8×10^{-3}.

E. Antenna Polarization Multiplexing

For wireless signal transmission, we can use antenna polarization multiplexing to increase the transmission capacity. Usually we define horizontal-polarization state and vertical-polarization state as H- and V-polarization, respectively. A few of dual- or three-polarization antennas are already commercially available at low frequencies (a few gigahertz) [65]. At high frequencies, such as W-band, the corresponding commercial product is also available although it is expensive [66]. We can use two single-polarization antennas to perform the function of a dual-polarization antenna, in order to realize antenna polarization multiplexing. Fig. 4 shows the schematic diagram of antenna polarization multiplexing [32]. There are two wavelength-division-multiplexing (WDM) channels, each of them carrying an optical baseband signal. After wavelength de-mutiplexing by a wavelength selective switch (WSS), we separate the two channels, which are denoted by channel 1 and channel 2, respectively. Then the signal carried by each channel will be up-converted to an electrical mm-wave signal by an optical heterodyne up-converter as described in Section IIB. The signal wireless transmission will be realized by a 4×4 MIMO including four transmitter horn antennas (HAs) and four receiver HAs. The upper two transmitter HAs and two receiver HAs are all horizontally polarized, and thus form an H-polarization HA array to deliver channel 1. Meanwhile, the lower two transmitter HAs and two receiver HAs are all vertically polarized, and thus form a V-polarization HA array to deliver channel 2. The signal baud rate as well as performance requirements for optical and wireless devices can be reduced by adopting antenna polarization multiplexing, but meanwhile double antennas and devices are required. The adoption of antenna polarization multiplexing can also increase wireless transmission capacity at the cost of stricter requirements for V-polarization [32].

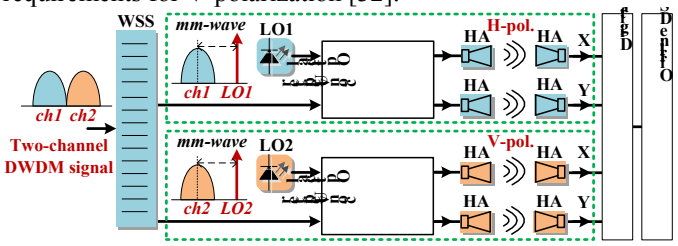

Fig. 4. Schematic diagram of fiber wireless integration system adopting antenna polarization multiplexing. WSS: wavelength selective switch, LO: local oscillator, HA: horn antenna.

F. High-Gain Mm-Wave Antenna

In the mm-wave communication system, the type and parameter of antennas plays an important role in communication performance. Mm-wave antenna usually has a relatively high gain. In practical applications, the antenna gain is usually the gain in the direction of the maximum radiation. The antenna gain can be expressed as [67]

$$G=4\pi A_e / \lambda^2 \tag{4}$$

Where A_e is the antenna effective area, that is, the ratio of the received power to the power density of the incident field, and $\lambda=c/f$ is the signal wavelength (c is the velocity of light, and f is the signal frequency). From Eq. 4, we can know that higher frequency causes shorter wavelength, which enables higher gain at the same antenna effective area. As a result, in the mm-wave band, it is not difficult to design high-gain antenna.

According to the Friis equation [68], the received power P_R can be expressed as

$$(P_R)dB=(P_T)dB+(G_T)dB+(G_R)dB-(L_P)dB \tag{5}$$

Where P_T denotes the transmitted power. G_T and G_R are the gain of transmitter antenna and receiver antenna, respectively. And L_P is the path loss and given as

$$(L_P)dB=20\log(4\pi d/\lambda) \tag{6}$$

Where d is the wireless transmission distance. The shorter the signal wavelength, the larger the path loss and the smaller the

received power. At the same time, in the mm-wave band, the loss of received power caused by high carrier frequency can be compensated by high-gain antenna, as shown in Eq. 5.

For the antennas with the same size, the higher the frequency, the narrower the beamwidth, so mm-wave antenna has a better performance in terms of anti-interception and anti-jamming. Because of its narrow beamwidth, mm-wave antenna is more suitable for point-to-point communication. Among many kinds of antennas, HA, parabolic antenna, and Cassegrain antenna (CA) are commonly used as mm-wave antennas [69-72]. HA is often used for short-range communications, while parabolic antenna and CA are used in long-distance communications due to their larger gain.

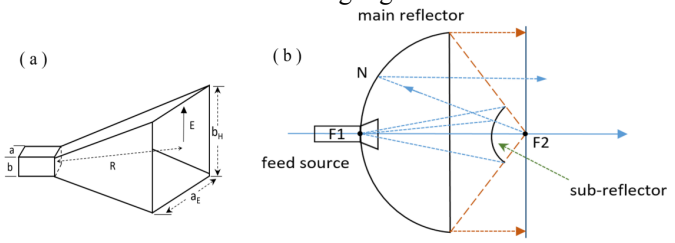

Fig. 5. (a) The schematic of HA; (b) the schematic of CA.

Fig. 5 shows the schematic of the rectangular HA and the CA, respectively. Rectangular HA, also known as the pyramidal HA, is made up of the rectangular waveguide E-plane and H-plane. As shown in Fig. 5(a), a and b represent the width and height of the rectangular waveguide, respectively; a_E and b_H denote the side length of the aperture on the E-plane and H-plane, respectively; R is the distance between the upper and lower horn aperture. The CA consists of a feed source, a parabolic main reflector and a hyperbolic subreflector, as shown in Fig. 5(b). F1 and F2 are two focal points of the hyperboloid and F2 is also the focal point of the paraboloid. First, the electromagnetic wave is emitted from the feed source, and then reflected via the hyperbolic subreflector to the parabolic main reflector. Finally, the main reflector radiates a plane beam with the same direction. The CA is evolved from a parabolic antenna with a higher aperture efficiency than a standard parabolic antenna and can be equivalent to a long-focal-length parabolic antenna, and thus it has a higher antenna gain [67].

In our experiment, the HA has 25-dBi gain [32] while the 1-foot W-band CA at 80GHz has 45-dBi gain [55].

G. Multi-Band Multiplexing

The employment of multi-band multiplexing can also reduce the signal baud rate at each band, which is similar to antenna polarization multiplexing. The penalty for this scheme is that more mm-wave devices are needed. In Ref. 73, we have experimentally demonstrated a photonics-aided all-band (D-, W-, and V-band) optical wireless integration system based on MIMO technique. We realized all-band PDM-QPSK wireless mm-wave signal transmission with the highest baud rate of over 100Gbaud (400Gb/s) up to now [73].

H. Broadband Mm-Wave Signal Detection

We can detect mm-wave signals by direct or heterodyne detection. Direct detection is commonly used in the mm-wave communication [74-77]. The structure of the direct detection scheme is shown in Fig. 6. At the receiver, we receive the wireless mm-wave signal by the antenna and then amplify it by the electrical amplifier. Then the high-frequency mm-wave signal is down-converted to the baseband signal by an envelope detector. The direct detection scheme is simple, low-cost and phase-noise insensitive [75]. But this scheme cannot detect the vector signal carried by the mm-wave but only intensity modulation signal. The theoretical derivation of the square-law detection in the direct detection scheme is as follows. The mm-wave signal received at the receiver can be expressed as

$$R(t)=\left[A+ms(t)\right]\cos\left(2\pi f_c t\right). \tag{7}$$

Where A represents the DC-bias in intensity modulation, $s(t)$ represents the intensity modulation signal, m represents the modulation index, and f_c represents the frequency of mm-wave. After the square-law detection, the output current of the envelope detector can be described as

$$\begin{aligned} I(t)&=\left|\left[A+ms(t)\right]\cos\left(2\pi f_c t\right)\right|^2 \\ &=\frac{1}{2}A^2+\frac{1}{2}Ams(t)+\frac{1}{2}m^2s^2(t)+\frac{1}{2}\left[A+ms(t)\right]^2\cos\left(4\pi f_c t\right). \end{aligned} \tag{8}$$

From Eq. 8, we can know that the first item is the DC component, the second item represents the component of the intensity modulation signal , the third item is the nonlinear noise, and the fourth item is the high-frequency component that needs suppressing. We can retrieve the intensity modulation signal linearly. The detected signal will suffer from the nonlinear noise and therefore be distorted. The output power of the envelope detector may be too small, so a baseband amplifier is needed. The direct detection system is relatively wasteful of power and bandwidth, but it is easy to implement and economical.

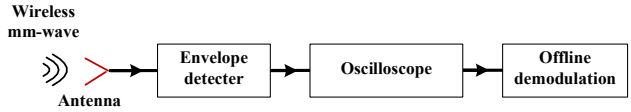

Fig. 6. The structure of the direct detection scheme.

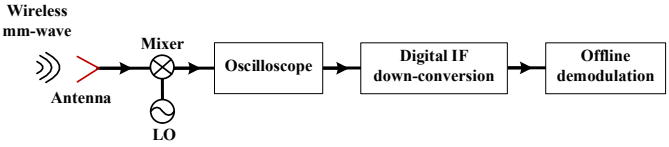

Fig. 7. The structure of the heterodyne detection scheme.

Heterodyne detection is also widely used in the mm-wave communication [78-82]. In contrast to the only one frequency in the homodyne detection, heterodyne means the beating of two or more frequencies at the receiver. For example, after the beating between two signals at frequencies f_1 and f_2, the new frequencies called heterodynes are created. One of the heterodynes is at the frequency f_1+f_2, and the other is at the frequency f_1-f_2. In order to realize the mm-wave down-conversion, the signal at low-frequency f_1-f_2 is reserved and the signal at high-frequency f_1+f_2 is filtered out.

The structure of the heterodyne detection scheme in the mm-wave communication is shown in Fig. 7. The scheme mainly consists of a RF LO and a mixer. After received by the antenna and amplified by the electrical amplifier, the wireless mm-wave signal combines with the RF LO signal in the mixer to achieve the mm-wave down-conversion. The down-

converted IF signal is captured by a digital storage oscilloscope and then digitally down-converted to the baseband signal. The heterodyne detection scheme requires an additional RF source and mixer resulting in a high cost, but the system has a high receiver sensitivity. This detection scheme can be used to detect both intensity modulation signal and vector signal, and the offline DSP algorithm can be used to compensate for the noise in the received signal. The theoretical derivation of the heterodyne detection scheme is as follows. The mm-wave vector signal received at the receiver can be expressed as

$$\mathrm{S}(t) = A\left[I(t)\sin\left(2\pi f_c t + \theta_c(t)\right) + Q(t)\cos\left(2\pi f_c t + \theta_c(t)\right)\right]. \quad (9)$$

Where A, f_c, and $\theta_c(t)$ represent the amplitude, frequency, and phase of the mm-wave signal, respectively. $I(t)$ and $Q(t)$ represent the I and Q components of the vector signal carried by the mm-wave, respectively.

The RF LO signal can be expressed as

$$\mathrm{S}_{\mathrm{LO}}(t) = A_{\mathrm{LO}}\cos\left(2\pi f_{\mathrm{LO}} t + \theta_{\mathrm{LO}}(t)\right). \quad (10)$$

Where A_{LO}, f_{LO}, and $\theta_{\mathrm{LO}}(t)$ represent the amplitude, frequency, and phase of the RF LO signal, respectively. The down-converted IF signal can be described as

$$\mathrm{S}_{\mathrm{IF}}(t) = A_{\mathrm{LO}}A\begin{bmatrix} I(t)\sin\left(2\pi f_c t - 2\pi f_{\mathrm{LO}} t + \theta_c(t) - \theta_{\mathrm{LO}}(t)\right) \\ +Q(t)\cos\left(2\pi f_c t - 2\pi f_{\mathrm{LO}} t + \theta_c(t) - \theta_{\mathrm{LO}}(t)\right)\end{bmatrix}. \quad (11)$$

The equation can be simplified as

$$\begin{aligned}\mathrm{S}_{\mathrm{IF}}(t) &= A_{\mathrm{LO}}A\left[I(t)\sin\left(2\pi f_{\mathrm{IF}} t + \theta_{\mathrm{IF}}(t)\right) + Q(t)\cos\left(2\pi f_{\mathrm{IF}} t + \theta_{\mathrm{IF}}(t)\right)\right] \\ &= -jA_{\mathrm{LO}}A\left[I(t) + jQ(t)\right]\exp\left(j2\pi f_{\mathrm{IF}} t + j\theta_{\mathrm{IF}}(t)\right).\end{aligned} \quad (12)$$

Where f_{IF} and $\theta_{\mathrm{IF}}(t)$ represent the frequency and phase of the down-converted IF signal, respectively. From Eq. 12, it can be seen that the transmitted vector signal $I(t)+jQ(t)$ will be recovered after the digital down-conversion and the phase correction in offline DSP.

Compared with the direct detection, the heterodyne detection is more complex and expensive, but the heterodyne detection based on DSP can effectively recover the distorted signal and show a higher receiver sensitivity. As a result, the heterodyne detection is more suitable for the ultra-broadband mm-wave communication.

III. Advanced DSP for Heterodyne Coherent Detection

In Section II, we have introduced a series of advanced enabling technologies, which are mainly used to improve the system structure of photonics-assisted broadband mm-wave communication. For a given system structure and certain available devices for the given system structure, advanced DSP will be further required to enhance the system performance. Since we mainly use heterodyne coherent detection in our demonstrated photonics-assisted broadband mm-wave communication systems, advanced coherent DSP algorithms used by the coherent optical transmission systems are also suitable for our demonstrated broadband mm-wave communication systems.

Fig. 8 shows the typical DSP algorithm flow diagram required by heterodyne coherent detection. First, the received IF signal is digitally down-converted to baseband before I/Q imbalance compensation based on the Gram-Schmidt orthogonal process (GSOP) algorithm [83]. Then the dispersion and nonlinearity [84, 85] impairments are compensated. Then the signal clock is recovered to get the best sample point [86]. Then polarization, antenna polarization, and PMD are recovered by the CMA algorithm [84-86]. Carrier recovery is divided into two steps. The fourth-power algorithm is used to estimate the frequency offset, and then the Viterbi-Viterbi phase estimation (VVPE) algorithm is used to eliminate the phase noise caused by the laser linewidth [86]. The algorithms for carrier recovery can tolerate larger laser linewidth and frequency jitter. Finally, a digital post filter combined with maximum likelihood sequence estimation (MLSE) [87] is used to eliminate the inter-symbol interference (ISI) before the decision and BER calculation.

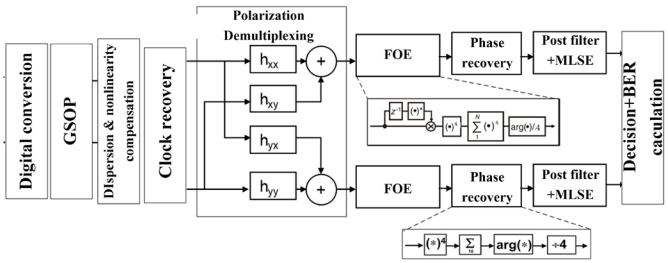

Fig. 8. DSP for heterodyne coherent detection.

In the following part of this Section, we will mainly introduce the advanced DSP algorithms used for fiber chromatic dispersion compensation, clock recovery, polarization demultiplexing and channel dynamic equalization, as well as carrier recovery. These DSP algorithms can be applied to both fiber-optics transmission systems and photonics-assisted mm-wave communication systems, to improve the receiver sensitivity and system performance. We will also introduce the DSP-based probabilistic constellation shaping technique. As one of the recent research hotspot, this technique can significantly enhance the system capacity and performance for both fiber-optics transmission systems and photonics-assisted mm-wave communication systems.

A. Fiber Chromatic Dispersion Compensation

When the optical baseband signal or optical mm-wave signal is transmitted in the fiber, the group velocity of different frequency components is not uniform, which can widen the signal in time domain and therefore deteriorate the signal quality. In the practical system, the dispersion will lead to the blur of eye diagram, the disappearance of clock component, the ISI and so on, which may cause the signal distortion. As a kind of static linear impairment [83, 86], the dispersion is constant for optical signals with a certain baud rate. Therefore, dispersion compensation is usually placed in the second step of DSP equalization. DSP-based dispersion compensation can be easily achieved by using time- or frequency-domain transfer function.

The principle of the electrical dispersion compensation in the time domain and frequency domain is shown in Figs. 9(a) and 9(b), respectively [85-88]. According to Ref. 83, the finite-impulse-response (FIR) tap coefficient a_k in the time-domain dispersion compensation is determined by the following equation

$$a_k = \sqrt{\frac{jcT^2}{D\lambda^2 z}} \exp(-j\frac{\pi cT^2}{D\lambda^2 z}k^2), \quad -\left\lfloor \frac{N}{2} \right\rfloor \leqslant k \leqslant \left\lfloor \frac{N}{2} \right\rfloor, \quad N = 2 \times \left\lfloor \frac{|D|\lambda^2 z}{2cT^2} \right\rfloor + 1. \tag{13}$$

Where D is the dispersion coefficient, λ is the signal wavelength, z is the length of the fiber, c is the velocity of light, T is the signal symbol duration, k is the tap number, and N is the tap order. For a certain wavelength and a certain dispersion coefficient, the size of N is determined by the fiber length and symbol duration. Therefore, for high-speed or long-distance optical signals, the value of N is larger, and the taps of the FIR filter and the calculation complexity are also increased.

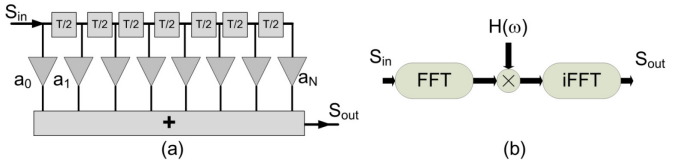

Fig. 9. Principle of electrical dispersion compensation in (a) time domain and (b) frequency domain.

Similarly, according to Ref. 83, the principle of frequency-domain dispersion compensation is relatively simple. According to the dispersion transfer function of the fiber channel, the dispersion can be directly compensated by multiplying the inverse transfer function, which can be expressed as

$$H(w) = \exp(j\frac{D\lambda^2 z}{4\pi c}\omega^2). \tag{14}$$

In our demonstrated photonics-assisted large-capacity/long-distance mm-wave signal transmission systems [37, 45, 54, 55, 108], we usually employ the single-mode fiber-28 (SMF-28) with a dispersion coefficient of 17ps/km/nm at 1550nm and frequency-domain electrical dispersion compensation. Since the SMF-28 transmission distance in our experimental systems is typically no more than 80km, we can ignore the nonlinear fiber transmission impairments, while frequency-domain electrical dispersion compensation can completely compensate for linear fiber dispersion impairment and EDFA can completely compensate for fiber transmission loss. As a result, in our experimental systems, fiber transmission usually causes negligible penalty.

B. Clock Recovery

The down-converted electrical signal at the receiver end can be converted to a digital signal by the ADC. However, in the practical system, since the local sampling clock is not synchronized with the transmitter signal clock, the sampling points of the ADC are usually not the best ones of the signal [89-92]. Furthermore, the instability of the local clock source may cause the sampling error of the system, which includes both the sampling phase error and the sampling frequency error. On the one hand, the clock error of the sampling points will introduce the ISI due to the imperfect sampling points. On the other hand, the sampling clock jitter can also cause signal performance fluctuations. Therefore, in order to realize the best digital signal recovery, the actual system needs to use the clock recovery module to eliminate the impact of the clock error. Considering that the dispersion will cause the disappearance of the clock component, the clock recovery module is usually placed after the dispersion compensation module, or cooperates with the dispersion compensation module to form a uniform equalization feedback module.

Actually, the clock recovery algorithm is a common requirement of communication systems and has been widely used in early wired and wireless communication systems [90-92]. In the optical communication systems, some classical clock recovery algorithms are also widely used, which proves the universality of these algorithms. Nowadays, in the coherent optical communication systems, the main clock recovery algorithms include feedforward and feedback ones, and the typical algorithms are presented as follows.

The square timing recovery algorithm was proposed by Martin [91]. This algorithm adopts a feedforward clock synchronization structure to realize the clock recovery. This algorithm redefines the clock and finds the best interpolation points by extracting the timing error phase of the signal asynchronous sampling sequence. This algorithm requires a resampling rate at four times of the signal baud rate and the calculation complexity is high.

The feedback time-domain clock recovery algorithm was proposed by Gardner [92]. This algorithm uses a feedback clock synchronization structure, which estimates the phase of the digital clock source by calculating timing error. The estimation of the timing error can track the frequency jitter of the signal, and therefore this algorithm can achieve dynamic clock recovery. Moreover, the Gardner clock recovery algorithm requires a resampling rate only at twice of the signal baud rate, and the algorithm complexity is low. This algorithm is widely used in the DSP modules of coherent optical communication systems.

Other common clock recovery algorithms include Godard algorithm [91] and Muller algorithm [90] and so on. In our demonstrated photonics-assisted large-capacity/long-distance mm-wave signal transmission systems [37, 45, 54, 55, 108], we mainly employ the square timing recovery algorithm and Gardner clock recovery algorithm.

C. Polarization Demultiplexing and Channel Dynamic Equalization

Since the fiber channel has a birefringence effect, in the coherent optical communication system with polarization multiplexing, polarization rotation occurs due to the randomness of the polarization state. Moreover, since the optical fiber is not perfect, the propagation constants of the two orthogonal polarization modes are different, which directly leads to a time delay between the two polarization modes, i.e., the PMD. The PMD is ever-changing in the practical fiber channel, and therefore we need dynamically equalize the channel and complete the polarization demultiplexing at the same time. The polarization-multiplexing system is actually a 2×2 MIMO structure, and therefore its polarization demultiplexing can use classical channel equalization algorithms, such as CMA and decision-directed least mean square (DD-LMS) algorithm.

The CMA algorithm was proposed by Godard et al. in 1980 [91]. As a blind equalization algorithm for QPSK signals, this

algorithm can also be applied to polarization-multiplexing coherent optical transmission systems. Ref. 91 has given a butterfly adaptive equalization filter structure for coherent optical transmission system with polarization multiplexing, which is shown in Fig. 10. This structure contains four adaptive filters to do channel estimation and signal equalization. h_{xx} and h_{yy} denote the equalization for single polarization itself. And the introduction of h_{xy} and h_{yx} takes the effects of polarization selection, polarization coupling, and PMD into consideration. The performance of the CMA algorithm depends on the number of taps and the convergence coefficients. The optimal number of taps and accurate convergence coefficients can be obtained by experimental investigation to reduce the algorithm complexity. In our demonstrated photonics-assisted large-capacity/long-distance mm-wave signal transmission systems [37, 38, 45, 54], additional CMA taps are required to suppress the potential wireless crosstalk existing in the wireless MIMO link, as mentioned in Section IIB.

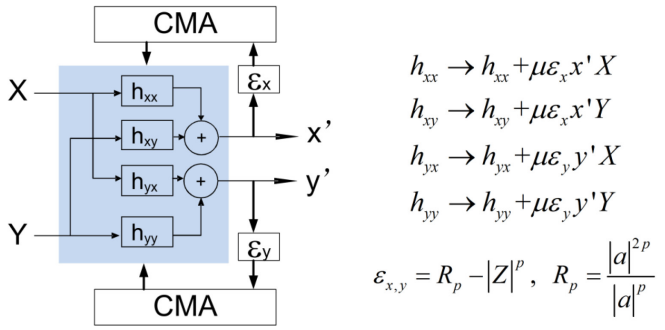

Fig. 10. The structure of the CMA algorithm and the updating formula of the tap coefficients.

For high-order modulation, such as 16QAM, 32QAM, and even higher-level QAM, many references also present dynamic equalization algorithms for them. Note that, since the update of the error function of the CMA aims at the single mode of QPSK, the error function cannot converge to zero for higher-level modulation formats, such as 16QAM, and therefore there is a larger error in the channel equalization. X. Zhou et al. proposed a cascaded multi-modulus algorithm (CMMA) for higher-level QAM, such as 8QAM and 16QAM [83]. This algorithm chooses the best decision value based on the different modulus radius of high-level QAM, which improves the accuracy of error function and makes it converge to zero. S. J. Savory et al. also experimentally verified the application of the radius-directed equalization (RDE) algorithm for 16QAM and higher-level QAM [83]. This algorithm carries out a continuous decision of modulus radius when calculating the error function, and finally chooses the modulus radius after decision as the calculation value of the error function. In addition, the commonly used polarization equalization algorithms also include independent component analysis (ICA) algorithm and so on [93]. DD-LMS can be also used for channel equalization, which needs to integrate carrier frequency and phase recovery into the feedback loop [83, 94]. Since it is more accurate with a slower convergence rate, DD-LMS is usually placed after the first-stage CMA or CMMA pre-convergence [95].

In our experimental demonstrations on photonics-assisted large-capacity vector mm-wave signal wireless transmission [11, 39, 47, 48, 55, 108, 109], we typically use CMMA equalization to realize multi-modulus recovery and signal polarization demultiplexing of the 16QAM and 64QAM vector mm-wave signals. As we know, with the increase of the modulation levels, the Euclidean distance of the QAM signals becomes shorter and shorter while their tolerance to noise becomes worse and worse. For the higher-level 64QAM vector mm-wave signal, we further use large-tap DD-LMS equalization after carrier recovery algorithm to converge each constellation points and eliminate the phase noise, in order to further improve the system performance [11, 47, 48]. Moreover, with the increase of the modulation levels of the QAM signals, higher receiver sensitivity and more transmitter power will be required. In order to solve this problem, we further introduce the technique of DSP-based probabilistic constellation shaping, which will be introduced in the following Section IIE. After the employment of the technique, we can reduce the required transmitter power of the higher-level QAM signals, and meanwhile enhance their tolerance to noise [108, 109].

D. Carrier Recovery

The carrier recovery usually includes frequency offset estimation and phase recovery. In a practical communication system, the LO frequency is not locked with the signal frequency, which may lead to a certain frequency offset from a few MHz to several hundred MHz or even GHz. Moreover, the signal light and the LO light will have a frequency drift effect due to the change of the environmental conditions including temperature. This frequency offset will lead to a large phase rotation of the signal light until covering the phase information of the signal itself. In addition, phase noise is introduced due to the laser linewidth, and it randomly changes at a certain rate, which can cause the tailing, extension, and aliasing of the constellation points. These two kinds of impairments will result in the deterioration of the signal quality.

In general, the carrier and phase recovery algorithms are divided into feedforward and feedback ones. Phase-locking loop (PLL) is a kind of classical feedback loop [83, 95], which can track the slow change of signal frequency and phase. However, with the increase of the optical transmission rate, the feedback carrier recovery algorithm sometimes cannot quickly track the signal change. The Viterbi-Viterbi algorithm [96] is a classic feedforward carrier phase recovery algorithm. According to the signal modulation format, this algorithm can eliminate the phase information after the *N*-th power of the signal, leaving only the frequency offset and phase noise. The frequency offset can be extracted and compensated after the correlation operation between neighboring symbols. The average of multiple symbols can reduce the effect of the amplified spontaneous emission (ASE) noise and improve the accuracy of phase noise estimation.

At present, the Viterbi-Viterbi algorithm has been widely used in carrier and phase recovery for QPSK and mPSK signals, as reported in Refs. 83-95. However, for 16QAM and higher-level QAM, the simple *N*-th power operation cannot completely eliminate the phase modulation of the signal. At the same time,

due to the different constellation radius, *N*-th power operation makes the subsequent direct phase extraction difficult. A constellation-partitioning algorithm was proposed to solve this problem [97]. This algorithm divides higher-level QAM constellations according to the radius of the constellation points, and therefore the constellation points with the same radius can be treated as mPSK signals. Therefore, the Viterbi-Viterbi algorithm can be used for carrier recovery in this scenario.

For mQAM signal, Pfau et al. proposed a simple and effective feedforward phase recovery algorithm, i.e., blind phase search (BPS) algorithm [98]. This algorithm pre-multiplies the signal by a recovery phase to do blind phase recovery. Then this algorithm calculates the Euclidean distance between the pre-recovery signal and the standard signal, and determines the best recovery phase by searching the smallest Euclidean distance. This algorithm only needs to change the decision function according to different constellation points, and therefore it is suitable for all constellation structures and has been widely used in high-level modulation formats, such as 16QAM, 64QAM and 1024QAM [99-102].

In our demonstrated photonics-assisted large-capacity/long-distance mm-wave signal transmission systems [11, 37, 39, 45, 47, 48, 54, 55, 108], we typically use the Viterbi-Viterbi algorithm to handle with the QPSK vector mm-wave signal. We use the constellation-partitioning algorithm combined with the Viterbi-Viterbi algorithm to handle with the 8QAM and 16QAM vector signals. We use the BPS algorithm to handle with the 64QAM vector mm-wave signal.

E. Probabilistic Constellation Shaping

Higher-level QAM modulation formats, such as 16QAM, 64QAM, and so on, have been widely investigated in fiber-optics transmission systems and photonics-assisted mm-wave systems to increase the spectral efficiency and transmission rate [9-11, 47-49]. However, the transmission distance or capacity of higher-level QAM signals are usually limited by power-constrained fiber-optics channel or power-insufficient wireless channel. Probabilistic constellation shaping, as one kind of coded modulation scheme and the recent research hotspot, can be used to extend the transmission distance or increase the capacity at the certain transmission distance for the higher-level QAM signals, without increasing the launch power into the fiber-optics or wireless channels [103-108].

In the probabilistic constellation shaping scheme, each dimension of the transmitted higher-level QAM signal constellations is distributed with non-equal probabilities following the Maxwell-Boltzmann distribution [103-106]. That is, the inner constellation points with lower energy are transmitted with a higher probability than the outer constellation points with higher energy. Fig. 11 gives a schematic illustration for the probabilistic constellation shaping for 16QAM. Therefore, the signal constellation after probabilistic shaping has a lower average power than the original one and therefore the transmitted power can be reduced. Although the probabilistic constellation shaping scheme will reduce the average bit number of QAM symbols and therefore reduce the effective bit rate, the saved energy is more than that used to compensate for the loss of the bit rate. In addition, the probabilistic constellation shaping scheme can enhance the noise tolerance of the system when the transmitted power is fixed since it can increase the effective Euclidean distance of the transmitted QAM signal constellations. Moreover, the coherent DSP algorithms, including those introduced in Sections IIIA-IIID, are also suitable for QAM signals after probabilistic constellation shaping [106-108], and therefore the DSP-based probabilistic constellation shaping scheme has a great flexibility to fiber-optics transmission systems and photonics-assisted mm-wave systems, without changing the existing system architecture and with little additional computation complexity.

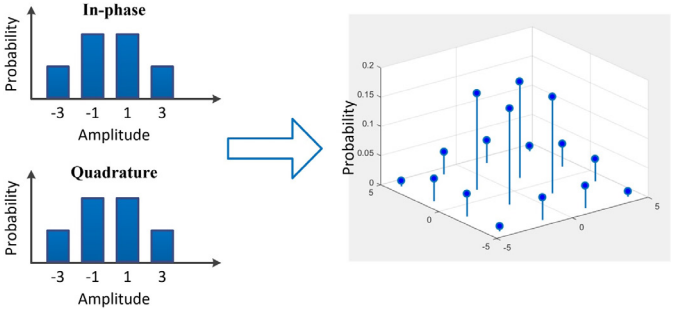

Fig. 11. A schematic illustration for the probabilistic constellation shaping for 16QAM.

We have introduced the technique of probabilistic constellation shaping into a photonics-assisted mm-wave signal transmission system at D-band, and experimentally demonstrated the employment of probabilistic constellation shaping can increase wireless transmission capacity by 1.5 times and wireless transmission distance by 2 times at the same time [109].

IV. Long-Distance and Large-Capacity Wireless Transmission of Vector Mm-Wave Signal

The transmission performance of the wireless mm-wave links is also key for the realization of photonics-assisted broadband mm-wave communication. Therefore in this Section, we will first do a theoretical analysis on the transmission performance of the wireless mm-wave links, to lay a foundation for the appropriate selection of the wireless mm-wave link for the given photonics-assisted broadband mm-wave communication systems. Then, enabled by the properly selected wireless mm-wave links, the enabling technologies introduced in Section II, and the advanced DSP introduced in Section III, we have experimentally demonstrated a series of long-distance and large-capacity wireless transmission of vector mm-wave signal, which will introduced in the second and third parts of this Section.

A. Theoretical Analysis on the Transmission Performance of Wireless Mm-Wave Links

When the wireless signal is transmitted in the atmospheric environment, it is needed to consider the impact of air on the absorption of the electromagnetic waves. Usually only a few of spectral windows with low absorptivity can be used. According to ITU-R P.676 [110], Fig. 12 gives the atmospheric loss of the

electromagnetic wave ranging from 1GHz to 300GHz in the cases of the dry air with ρH_2O = 0g/m^3 and the wet air with ρH_2O = 7.5g/m^3, respectively.

It can be seen from Fig. 12 that, some H_2O or O_2 peaks with a relatively high loss caused by spectrum absorption exist in the frequencies of 23GHz, 60GHz, 119GHz and 183GHz. The absorption is caused by the interaction between the electromagnetic wave and the water vapor or oxygen. The atmospheric loss of 60GHz and 183GHz is 14.5dB/km and 27.7dB/km in the case of the wet air with ρH2O = 7.5g/m^3, respectively. Therefore, these two carrier frequencies are only suitable for short-distance communication applications.

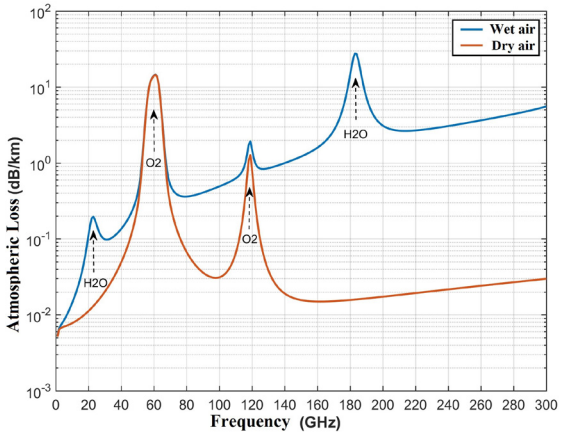

Fig. 12. The atmospheric absorption loss over 1GHz-300GHz.

Table 1. Parameters of four mm-wave bands.

Band	Frequency range (GHz)	Antenna gain (dBi)	Beamwidth (°)	Carrier frequency (GHz)	Atmospheric loss (dB/km)
Q	33-50	25	10	38	0.12
V	50-75	37	2.5	60	14.5
E	71-76 /81-86	45	0.8	74	0.39
W	75-110	45	0.8	83,90,100	0.38,0.41 ,0.49

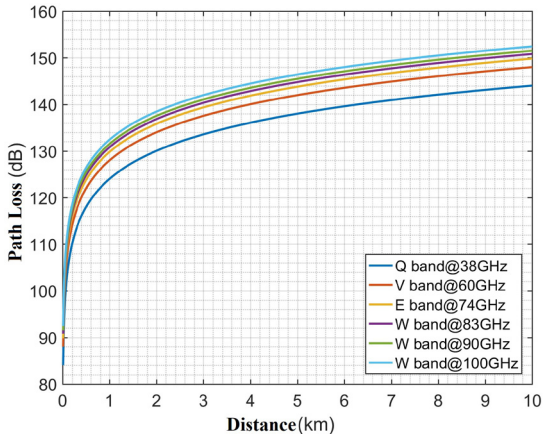

Fig. 13. The curve of the relationship between free-space path loss and transmission distance.

Taking the impact of both atmospheric loss and free-space path loss into consideration, the received power is

$$(P_R)dB = (P_T)dB + (G_T)dB + (G_R)dB - (L_P)dB - (L_f)dB - (d \times L_a)dB. \quad (15)$$

Where P_R and P_T denote the received power and transmitted power, respectively. G_T and G_R denote the gain of transmitter antenna and receiver antenna, respectively. L_P denotes the free-space path loss. L_f denotes the loss of antenna feedline. L_a denotes the atmospheric loss factor, while d denotes the wireless transmission distance. According to the experimental conditions, the Q-band (33-50GHz), V-band (50-75GHz), E-band (71-76GHz / 81-86GHz), and W-band (75-110GHz) are chosen to do the performance analysis for the mm-wave link. The used antennas are the standard HA, lens HA, and CA. The parameters of these mm-wave bands are shown in Table 1, where the carrier frequency is the operating frequency of the selected mm-wave link. According to the parameters in Table 1 and Eq. 15, the free-space path loss is given in Fig. 13. With the increase of the transmission distance d, the free-space path loss increases, and the decay rate is relatively high when the distance d is less than 1km. At the same distance, the higher the frequency, the greater the loss.

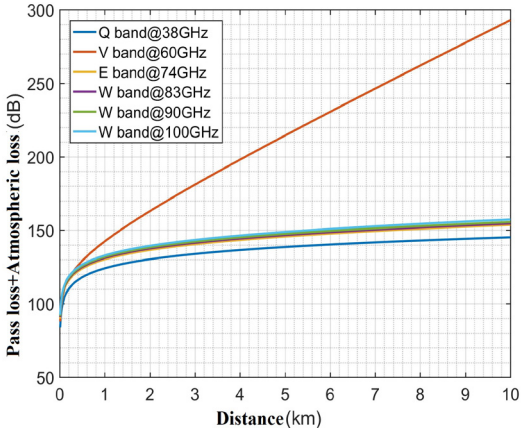

Fig. 14. The curve of the free-space path loss combined with the atmospheric loss versus the transmission distance.

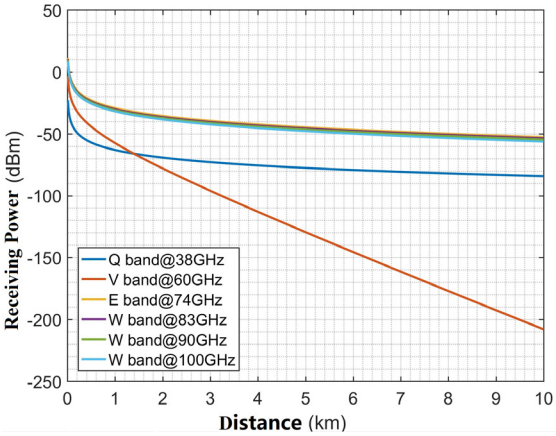

Fig. 15. The relationship between the received power and the transmission distance.

Fig. 14 gives the free-space path loss combined with the atmospheric loss versus the transmission distance. Due to the severe attenuation caused by the oxygen absorption peak, the loss of the V-band is dominated by the atmospheric loss when the transmission distance is longer than 400m, and it tends to increase linearly as the transmission distance increases. However, the atmospheric loss of the Q-band, E-band, and W-band is small, and it is not obvious compared with the path loss

and even can be ignored within a certain distance. The relationship between the received power and the transmission distance is shown in Fig. 15 based on Eq. 15, where the transmitted power P_T is 16dBm and the loss of antenna feedline L_f is set to 5dB.

Similarly, the V-band is severely attenuated by the atmosphere, resulting in a great decrease of the received power when the transmission distance increases. However, the received power of the E-band and W-band is higher than the Q-band, because of the use of a 45-dBi high-gain antenna. It can be seen from Eq. 4 that the higher frequency and shorter wavelength lead to a higher antenna gain with the same size. Therefore, the high path loss caused by high frequency can be compensated by the high-gain antenna.

According to the aforementioned analysis, it can be seen that, the W-band, with 35-GHz wide bandwidth, is located in the window with lower atmospheric loss, and its atmospheric loss over the whole band is less than 0.5dB/km. Therefore, W-band is suitable for long-distance wireless transmission. Ref. 111 has verified the budget and transmission capacity of the W-band link, and experimentally demonstrated the wireless transmission at W-band with distances of 800m, 1.2km, and 4.4km. The received power is -19.77dBm, -30.85dBm, and -29.61dBm, respectively. Considering the influence of connection loss, environmental multipath interference, imperfect antenna alignment, and measurement error, the error between theoretical budget and experimental measurement is less than 6dB. The experimental results show that the W-band possesses the capability of long-distance wireless transmission.

B. Experimental Demonstrations on Large-Capacity Vector Mm-Wave Signal Wireless Transmission over Long Distance

Our experimental demonstrations on large-capacity vector mm-wave signal wireless transmission over long distance are mainly located at the W-band from 75GHz to 110GHz as well as K-band from 18GHz to 27GHz [55, 79, 112, 113].

K-band has lower atmospheric loss than W-band, and the components at this band are much cheaper and more mature compared to those at W-band. We experimentally demonstrated up to 32-Gb/s 16QAM signal transmission over 100-km SMF-28 and >1-km wireless air 2×2 MIMO link at K-band [113]. The power amplifier at the wireless transmitter end has 31-dB gain, 31-dBm saturation output power, and 17-GHz~27-GHz operating frequency range. Relative to the amplifier at W-band, this RF power amplifier has higher output power. The K-band CA has a ~34-dBi gain, a ~2.9° 3-dB beamwidth, <1-ft diameter, <30-dB cross polarization discrimination, and an operating frequency range of 21.2~23.6 GHz. The received K-band RF signal is boosted by RF amplifier with an operating frequency range of DC~60GHz and a gain over 35dB. The recorded data by a high-speed real-time oscilloscope is processed offline based on advanced DSP [114]. In order to eliminate the phase noise and converge each constellation points as well as compensate for the potential multi-path effects, we use 113-tap T-spaced DD-LMS equalization. After transmission over 1-km wireless distance, the BER is smaller than 3.8×10^{-3}.

At W-band, we have realized 20-Gb/s and 40-Gb/s signal transmission over 640-m and 160-m wireless distance, respectively, based on high-receiver-sensitivity QPSK modulation, 2×2 MIMO, high-gain antenna of 35dBi, and heterodyne detection with advanced DSP [112]. After adding a power amplifier with 20-dBm saturation output power at the wireless transmitter end, we further realized 20-Gb/s QPSK signal transmission at W-band over 1.7-km wireless distance [79]. Compared to QPSK, 8QAM has a higher spectral efficiency and can reduce the bandwidth requirement for optical and electrical components. Recently, using the similar architecture as that in [79] and 8QAM modulation, we have realized 54-Gb/s signal transmission at W-band over 2.5-km wireless distance [55]. We also realized bi-directional transmission of K-band and W-band signals over 2.5-km wireless distance. The bit rate of the K-band link is 32Gb/s with 16QAM modulation, while the bit rate of the W-band link is 54Gb/s with 8QAM modulation [55].

C. Experimental Demonstrations on Ultra-Large-Capacity Vector Mm-Wave Signal Wireless Transmission

Since 2012, we have gradually increased the wireless transmission capacity of the photonics-assisted mm-wave signal communication systems from 100Gb/s to 400Gb/s, finally to 1Tb/s [37, 52, 108, 114]. The enhancement of the wireless transmission capacity is mainly due to the realization and seamless integration of various enabling technologies introduced in Section II and various advanced DSP introduced in Section III, at different mm-wave bands, including Q-band, V-band, W-band, D-band, and so on.

In 2012, based on 2×2 MIMO, photonics-assisted QPSK vector mm-wave signal generation, heterodyne detection with advanced DSP, we realized 108-Gb/s signal wireless delivery over 1-m distance, which was the first time to realize signal transmission over 100Gb/s at W-band [37].

In 2013, we realized 400-Gb/s signal wireless delivery based on Q- and W-band multiplexing [52]. In our demonstrated system, we can simultaneously deliver 2×112-Gb/s dual-channel PDM-16QAM wireless signal at Q-band and 2×108-Gb/s dual-channel PDM-QPSK wireless signal at W-band through a 4×4 MIMO wireless link with wireless distance of ~1m [52].

In 2014, we further realized 432-Gb/s wireless signal delivery at W-band [114]. In this experimental demonstration, we used a 4×4 MIMO architecture, photonics-assisted 16QAM vector mm-wave signal generation at 27Gbaud, antenna polarization multiplexing, and heterodyne detection based on advanced DSP. After wireless delivery over 2-m distance, the measured BER is smaller than 3.8×10^{-3} [114].

In 2018, we experimentally demonstrated the wireless transmission of D-band 64QAM mm-wave signals over 3.1-m distance with a total bit rate of 1.056Tb/s and a BER under 4×10^{-2}, employing photonics-assisted technology, probabilistic constellation shaping, wireless MIMO, and advanced DSP [108]. To the best of our knowledge, this creates a new record for ultra-large-capacity vector mm-wave signal wireless transmission.

We also demonstrated over 100-Gb/s wireless signal delivery at Q-, V-, W-, and D-band [32, 46-48, 73]. At lower frequencies, such as Q- or V-band, although the bandwidth is smaller than that at W- or D-band, we can use high-order QAM, such as 64QAM, to improve spectral efficiency, because we can

easily get more output power at lower frequencies [47, 48]. At Q- or V-band, we can get a maximal output power up to 30dBm, and therefore the SNR at the receiver is higher and we can realize high-order QAM detection.

V. Conclusions

In this paper, we review key enabling technologies and advanced DSP for photonics-assisted broadband mm-wave communication. The key enabling technologies we developed mainly focus on the improvement of the system structure, while our design in advanced DSP can further enhance the system performance for a given system structure and commercially available devices. All the key enabling technologies and advanced DSP have been verified by a series of experimental demonstrations on large-capacity/long-distance vector mm-wave signal wireless transmission. Particularly, in terms of ultra-large-capacity vector mm-wave signal wireless transmission, we have realized a record of >1-Tb/s wireless mm-wave signal transmission at D-band based on advanced 64QAM modulation, probabilistic constellation shaping, 4×4 MIMO reception with antenna polarization multiplexing, and heterodyne detection with advanced DSP. In terms of ultra-long-distance vector mm-wave signal wireless transmission, we have realized a milestone 54-Gb/s wireless mm-wave signal transmission over 2500m at W-band employing advanced 8QAM modulation, 2×2 MIMO reception with antenna polarization multiplexing, high gain CA, and heterodyne detection with advanced DSP. We believe these findings will form the basis for the development, standardization and final implementation of ultra-high-speed fiber-wireless integration communication systems to meet the eMBB challenges in 5G.

References

1. J. G. Andrews, S. Buzzi, W. Choi, S. V. Hanly, A. Lozano, A. C. K. Soong, and J. C. Zhang, "What will 5G be?," *IEEE J. on Selected Areas in Communications*, vol. 32, no. 6, pp. 1065-1082, 2014.
2. E. Gustafsson and A. Jonsson, "Always best connected," *IEEE Wireless Communications*, vol. 10, no. 1, pp. 49-55, 2003.
3. F. Lu, L. Cheng, M. Xu, J. Wang, S. Shen, and G. K. Chang, "Orthogonal and sparse chirp division multiplexing for MMW fiber-wireless integrated systems," *IEEE Photon. Technol. Lett.*, vol. 29, no. 16, pp. 1316-1319, 2017.
4. G. Liu, X. Hou, J. Jin, F. Wang, Q. Wang, Yue Hao, Yuhong Huang, X. Wang, X. Xiao, and A. Deng, "3-D-MIMO with massive antennas paves the way to 5G enhanced mobile broadband: from system design to field trials," *IEEE J. on Selected Areas in Communications*, vol. 35, no. 6, pp. 1222-1233, 2017.
5. T. S. Rappaport, S. Sun, R. Mayzus, H. Zhao, Y. Azar, K. Wang, G. N. Wong, J. K. Schulz, M. Samimi, and F. Gutierrez, "Millimeter wave mobile communications for 5G cellular: It will work!," *IEEE Access*, vol. 1, pp. 335-349, 2013.
6. M. Xu, J.-H. Yan, J. Zhang, F. Lu, J. Wang, L. Cheng, D. Guidotti, and G.-K. Chang, "Bidirectional fiber-wireless access technology for 5G mobile spectral aggregation and cell densification," *J. of Optical Communications and Networking*, vol. 8, no. 12, pp. B104-B110, 2016.
7. F. Lu, M. Xu, L. Cheng, J. Wang, J. Zhang, and G.-K. Chang., "Non-orthogonal multiple access with successive interference cancellation in millimeter-wave radio-over-fiber systems," *J. Lightw. Technol.*, vol. 34, no. 17, pp. 4179-4186, 2016.
8. M. Xu, J. Zhang, F. Lu, J. Wang, L. Cheng, D. Guidott, and G.-K. Chang, "Orthogonal multiband CAP modulation based on offset-QAM and advanced filter design in spectral efficient MMW RoF systems," *J. Lightw. Technol.*, vol. 35, no. 4, pp. 997-1005, 2017.
9. X. Zhou, L. E. Nelson, and P. Magill, "Rate-adaptable optics for next generation long-haul transport networks," *IEEE Communications Magazine*, vol. 51, no. 3, pp. 41-49, 2013.
10. A. Sano, T. Kobayashi, K. Ishihara, H. Masuda, S. Yamamoto, K. Mori, E. Yamazaki, E. Yoshida, Y. Miyamoto, T. Yamada, and H. Yamazaki, "240-Gb/s polarization-multiplexed 64-QAM modulation and blind detection using PLC-LN hybrid integrated modulator and digital coherent receiver," *Proc. ECOC2009*, Vienna, Austria, PD2.2.
11. X. Li, J. Yu, Y. Xu, X. Pan, F. Wang, Z. Li, B. Liu, L. Zhang, X. Xin, and G. K. Chang, "60-Gbps W-band 64QAM RoF system with T-spaced DD-LMS equalization," *Proc. OFC 2017*, Los Angeles, California, M3E.2.
12. J. Zhang, J. Yu, N. Chi, Z. Dong, X. Li, Y. Shao, and L. Tao, "Multichannel optical frequency-locked multicarrier source generation based on multichannel recirculation frequency shifter loop," Opt. Lett., vol. 37, no. 22, pp. 4714-4716, 2012.
13. X. Li, J. Yu, Z. Dong, J. Zhang, Y. Shao, and N. Chi, "Multi-channel multi-carrier generation using multi-wavelength frequency shifting recirculating loop," Opt. Express, vol. 20, no. 20, pp. 21833-21839, 2012.
14. X. Li and J. Yu, "W-band RoF transmission based on optical multi-carrier generation by cascading one directly-modulated DFB laser and one phase modulator," Opt. Commun., vol. 345, pp. 80-85, 2015.
15. J. Yu, Z. Jia, T. Wang, and G. K. Chang, "Centralized lightwave radio-over-fiber system with photonic frequency quadrupling for high frequency millimeter-wave generation," *IEEE Photon. Technol. Lett.*, vol. 19, no. 19, pp. 1499-1501, 2007.
16. J. Yu, Z. Jia, L. Yi, Y. Su, G.-K. Chang, and T. Wang, "Optical millimeter-wave generation or up-conversion using external modulators," *IEEE Photon. Technol. Lett.*, vol. 18, no. 1, pp. 265-267, 2006.
17. M. Mohamed, X. Zhang, B. Hraimel, and K. Wu, "Analysis of frequency quadrupling using a single Mach-Zehnder modulator for milli-meterwave generation and distribution over fiber systems," *Opt. Express*, vol. 16, no. 14, pp. 10786-10802, 2008.
18. G. Qi, J. Yao, J. Seregelyi, S. Paquet, and C. Belisle, "Optical generation and distribution of continuously tunable millimeter-wave signals using an optical phase modulator," *J. Lightw. Technol.*, vol. 23, no. 9, pp. 2687-2695, 2005.
19. X. Hu, L. Zhang, P. Cao, and Y. Su, "Filter-less frequency quadrupling technique for optical millimeter-wave signal generation based on one single-drive Mach-Zehnder modulator," *Proc. PGC 2010*, Singapore, pp. 1-2.
20. X. Li, J. Yu, J. Zhang, J. Xiao, Z. Zhang, Y. Xu, and L. Chen, "QAM vector signal generation by optical carrier suppression and precoding techniques," *IEEE Photon. Technol. Lett.*, vol. 27, no. 18, pp. 1977-1980, 2015.
21. Y. Wang, Y. Xu, X. Li, J. Yu, and N. Chi, "Balanced precoding technique for vector signal generation based on OCS," *IEEE Photon. Technol. Lett.*, vol. 27, no.13, pp. 2469-2472, 2015.
22. X. Li, J. Zhang, J. Xiao, Z. Zhang, Y. Xu, and J. Yu, "W-band 8QAM vector signal generation by MZM-based photonic frequency octupling," *IEEE Photon. Technol. Lett.*, vol. 27, no. 12, pp. 1257-1260, 2015.
23. J. Xiao, Z. Zhang, X. Li, Y. Xu, L. Chen, and J. Yu, "High-frequency photonic vector signal generation employing a single phase modulator," *IEEE Photon. J.*, vol. 7, no. 2, pp. 7101206, 2015.
24. X. Li, J. Yu, and G.-K. Chang, "Frequency-quadrupling vector mm-wave signal generation by only one single-drive MZM," *IEEE Photon. Technol. Lett.*, vol. 28, no. 12, pp. 1302-1305, 2016.
25. L. Zhao, J. Yu, L. Chen, P. Min, J. Li, and R. Wang, "16QAM vector millimeter-wave signal generation based on phase modulator with photonic frequency doubling and precoding," *IEEE Photonics Journal*, vol. 8, no. 2, pp. 5500708, 2016.
26. X. Li, Y. Xu, and J. Yu, "Single-sideband W-band photonic vector millimeter-wave signal generation by one single I/Q modulator," *Opt. Lett.*, vol. 41, no. 18, pp. 4162-4165, 2016.
27. H. C. Chien, Z. Jia, J. Zhang, Z. Dong, and J. Yu, "Optical independent-sideband modulation for bandwidth-economic coherent transmission," *Opt. Express*, vol. 22, no. 8, pp. 9465-9470, 2014.
28. L. Zhang, T. Zuo, Q. Zhang, E. Zhou, G. N. Liu, and X. Xu, "Transmission of 112-Gb/s+ DMT over 80-km SMF enabled by twin-SSB technique at 1550nm," *Proc. ECOC 2015*, Valencia, We4.6.4.

29. Z. Xu, R. Hui, and M. O'Sullivan, "Dual-band OOFDM system based on tandem single-sideband modulation transmitter," *Opt. Express*, vol. 17, no. 16, pp. 13479-13486, 2009.
30. L. Zhang, Q. Zhang, T. Zuo, E. Zhou, G. N. Liu and X. Xu, "C-band Single Wavelength 100-Gb/s IM-DD Transmission over 80-km SMF without CD compensation using SSB-DMT," *Proc. OFC 2015*, Los Angeles, California, Th4A2.
31. J. Ma, J. Yu, C. Yu, X. Xin, J. Zeng, and L. Chen, "Fiber dispersion influence on transmission of the optical millimeter-waves generated using LN-MZM intensity modulation," *J. Lightw. Technol.*, vol. 25, no. 11, pp. 3244-3256, 2007.
32. J. Yu, X. Li, and N. Chi, "Faster than fiber: over 100-Gb/s signal delivery in fiber wireless integration system," *Optics Express*, vol. 21, no.19, pp. 22885-22904, 2013.
33. X. Li and J. Yu, "2 × 2 multiple-input multiple-output optical-wireless integration system based on optical independent-sideband modulation enabled by an in-phase/quadrature modulator," *Opt. Lett.*, vol. 41, no. 13, pp. 3138-3141, 2016.
34. N. Cvijetic, D. Qian, J.Yu, Y. K. K. Huang, and T. Wang, "Polarization-multiplexed optical wireless transmission with coherent detection," *J. Lightw. Technol.*, vol. 28, no. 8, pp. 1218-1227, 2010.
35. L. Tao, Z. Dong, J. Yu, N. Chi, J. Zhang, X. Li, Y. Shao, and G. K. Chang, "Experimental demonstration of 48-Gb/s PDM-QPSK radio-over-fiber system over 40-GHz mm-wave MIMO wireless transmission," *IEEE Photon. Technol. Lett.*, vol. 24, no. 24, pp. 2276-2279, 2012.
36. X. Li, J. Yu, Z. Dong, Z. Cao, N. Chi, J. Zhang, Y. Shao, and L. Tao, "Seamless integration of 57.2-Gb/s signal wireline transmission and 100-GHz wireless delivery," *Opt. Express*, vol. 20, no. 22, pp. 24364-24369, 2012.
37. X. Li, Z. Dong, J. Yu, N. Chi, Y. Shao, and G. K. Chang, "Fiber wireless transmission system of 108-Gb/s data over 80-km fiber and 2×2 MIMO wireless links at 100GHz W-Band frequency," *Opt. Lett.*, vol. 37, no. 24, pp. 5106-5108, 2012.
38. X. Li, J. Yu, Z. Dong, J. Zhang, N. Chi, and J. Yu, "Investigation of interference in multiple-input multiple-output wireless transmission at W band for an optical wireless integration system," *Opt. Lett.*, vol. 38, no. 5, pp. 742-744, 2013.
39. Z. Dong, J. Yu, X. Li, G. K. Chang, and Z. Cao, "Integration of 112-Gb/s PDM-16QAM wireline and wireless data delivery in millimeter wave RoF system," *Proc. OFC 2013*, Anaheim, California, OM3D.2.
40. T. Kuri, H. Toda, J. J. V. Olmos, and K. I. Kitayama, "Fiber-wireless DWDM networks and radio-over-fiber technologies," *Proc. MWP 2009*, Valencia, pp. 1-4.
41. C. Liu, H. C. Chien, S. H. Fan, J. Yu, and G. K. Chang, "Enhanced vector signal transmission over double-sideband carrier-suppressed optical millimeter-waves through a small LO feedthrough," *IEEE Photon. Technol. Lett.*, vol. 24, no. 3, pp. 173-175, 2012.
42. X. Li, J. Yu, Z. Dong, J. Zhang, L. Tao, N. Chi, and Y. Shao, "Performance improvement by pre-equalization in W-band (75-110GHz) RoF system," *Proc. OFC 2013*, Anaheim, California, OW1D.3.
43. X. Li, J. Yu, N. Chi, Z. Dong, J. Zhang, and J. Yu, "The reduction of the LO number for heterodyne coherent detection," *Opt. Express*, vol. 20, no. 28, pp. 29613-29619, 2012.
44. X. Li, Z. Dong, J. Yu, J. Yu, and N. Chi, "Heterodyne coherent detection of WDM PDM-QPSK signals with spectral efficiency of 4b/s/Hz," *Opt. Express*, vol. 21, no. 7, pp. 8808-8814, 2013.
45. X. Li, J. Yu, and J. Xiao, "Demonstration of ultra-capacity wireless signal delivery at W-band," *J. Lightw. Technol.*, vol. 34, no. 1, pp. 180-187, 2016.
46. X. Li and J. Yu, "Over 100 Gb/s ultrabroadband MIMO wireless signal delivery system at the D-band," *IEEE Photon. J.*, vol. 8, no. 5, pp. 7906210, 2016.
47. X. Li, Y. Xu, and J. Yu, "Over 100-Gb/s V-band single-carrier PDM-64QAM fiber-wireless-integration system," *IEEE Photon. J.*, vol. 8, no. 5, pp. 7906907, 2016.
48. X. Li and J. Yu, "Generation and heterodyne detection of >100-Gb/s Q -band PDM-64QAM mm-wave signal," *IEEE Photon. Technol. Lett.*, vol. 29, no. 1, pp. 27-30, 2017.
49. J. Yu and X. Zhou, "Ultra-high-capacity DWDM transmission system for 100G and beyond," *Commun. Mag.*, vol. 48, pp. S56-S64, 2010.
50. X. Zhou, J. Yu, M. Huang, Y. Shao, T. Wang, P. Magill, M. Cvijetic, L. Nelson, M. Birk, G. Zhang, S. Y. Ten, H. B. Matthew, and S. K. Mishra, "32Tb/s (320x114Gb/s) PDM-RZ-8QAM transmission over 580km of SMF-28 ultra-low-loss fiber," *Proc. OFC 2009*, San Diego, California, PDPB4.
51. J. Zhang, J. Yu, N. Chi, Z. Dong, X. Li, and G. K. Chang, "Multichannel 120-Gb/s data transmission over 2 × 2 MIMO fiber-wireless link at W-band," *IEEE Photon. Technol. Lett.*, vol. 25, no. 8, pp. 780-783, 2013.
52. X. Li, J. Yu, J. Zhang, Z. Dong, F. Li, and N. Chi, "A 400G optical wireless integration delivery system," *Opt. Express*, vol. 21, no. 16, pp. 18812-18819, 2013.
53. Z. Jia, H. C. Chien, J. Zhang, Y. Cai, and J. Yu, "Performance comparison of dual-carrier 400G with 8/16/32-QAM modulation formats," *IEEE Photon. Technol. Lett.*, vol. 27, no. 13, pp. 1414-1417, 2015.
54. X. Li, J. Xiao, and J. Yu, "Long-distance wireless mm-wave signal delivery at W-band," *J. Lightw. Technol.*, vol. 34, no. 2, pp. 661-668, 2016.
55. X. Li, J. Yu, K. Wang, Y. Xu, L. Chen, L. Zhao, and W. Zhou, "Bidirectional delivery of 54-Gbps 8QAM W-band signal and 32-Gbps 16QAM K-band signal over 20-km SMF-28 and 2500-m wireless distance," *Proc. OFC 2017*, Los Angeles, California, Th5A.7.
56. J. Zhang, M. Xu, J. Wang, F. Lu, L. Cheng, H. Cho, K. Ying, J. Yu, and G.-K. Chang, "Full-duplex quasi-gapless carrier aggregation using FBMC in centralized radio-over-fiber heterogeneous networks," *J. Lightwave Technol.*, vol. 35, no. 4, pp. 989-996, 2017.
57. J. Yu and J. Zhang, "Recent progress on high-speed optical transmission," *Digital Communications and Networks*, vol. 2, no. 2, pp. 65-76, 2016.
58. J. Zhang and J. Yu, "Single-Carrier 400G Based on 84-GBaud PDM-8QAM Transmission over 2,125 km SSMF Enhanced by Pre-Equalization, LUT and DBP," *Proc. OFC 2017*, Los Angeles, California, Tu2E. 2.
59. F. Li, Z. Cao, X. Li, Z. Dong, and L. Chen, "Fiber-wireless transmission system of PDM-MIMO-OFDM at 100 GHz frequency," *J. Lightw. Technol.*, vol. 31, no. 14, pp. 2394-2399, 2013.
60. F. Li, J. Yu, Z. Cao, J. Xiao, H. Chen, and L. Chen, "Reducing the peak-to-average power ratio with companding transform coding in 60 GHz OFDM-ROF systems," *J. Opt. Commun. Netw.*, vol. 4, no. 3, pp. 202-209, 2012.
61. L. Tao, J. Yu, Y. Fang, J. Zhang, Y. Shao, and N. Chi, "Analysis of noise spread in optical DFT-S OFDM systems," *J. Lightwave Technol.*, vol. 30, no. 20, pp. 3219-3225, 2012.
62. Q. Yang, Z. He, Z. Yang, S. Yu, X. Yi, and W. Shieh, "Coherent optical DFT-spread OFDM transmission using orthogonal band multiplexing," *Opt. Express*, vol. 20, no. 3, pp. 2379-2385, 2012.
63. Y. Tang, W. Shieh, and B. S. Krongold, "DFT-Spread OFDM for fiber nonlinearity mitigation," *IEEE Photon. Technol. Lett.*, vol. 22, no. 16, pp. 1250-1252, 2010.
64. L. Tao, J. Yu, Q. Yang, M. Luo, Z. He, Y. Shao, J. Zhang, and N. Chi, "Spectrally efficient localized carrier distribution scheme for multiple-user DFT-S OFDM RoF- PON wireless access systems," *Opt. Express*, vol. 20, no. 28, pp. 29665-29672, 2012.
65. http://www.radiowaves.com/en/product/hplpd1-38.
66. http://www.mwavellc.com/commercial/80-GHz-Dual-Polarization-Adapter.php.
67. C. A. Balanis, "Antenna theory: analysis and design," John Wiley & Sons, 2016.
68. H. T. Friis and T. Harald, "A note on a simple transmission formula," *Proceedings of the Institute of Radio Engineers*, vol. 34, no. 5, pp. 254-256, 1946.
69. X. Li, J. Yu, J. Zhang, Z. Dong, and N. Chi, "Doubling transmission capacity in optical wireless system by antenna horizontal-and vertical-polarization multiplexing," *Opt. Lett.*, vol. 38, no. 12, pp. 2125-2127, 2013.
70. M. Schlechtweg and A. Tessmann, "From 100 GHz to terahertz electronics - Activities in Europe," *Proc. CSIC 2006*, San Antonio, TX, pp. 8-11.
71. V. Dyadyuk, J. D. Bunton, and Y. J. Guo, "Study on high rate long range wireless communications in the 71-76 and 81-86 GHz bands," *Proc. EuMC 2009*, pp. 1315-1318.

72. T. P. McKenna, A. N.Jeffrey, and R. C. Thomas, "Experimental demonstration of photonic millimeter-wave system for high capacity point-to-point wireless communications," *J. Lightw. Technol.*, vol. 32, no. 20, pp. 3588-3594, 2014.
73. X. Li, J. Yu, J. Xiao, Y. Xu, and L. Chen, "Photonics-aided over 100-Gbaud all-band (D-, W- and V-band) wireless delivery," *Proc. ECOC 2016*, Düsseldorf, Germany, pp. 303-305.
74. M. Chen, X. Xiao, J. Yu, X. Li, and F. Li, "Real-time generation and reception of OFDM signals for X -band RoF uplink with heterodyne detection," *IEEE Photon. Technol. Lett.*, vol. 29, no. 1, pp. 51-54, 2017.
75. C.-H. Li, M.-F. Wu, C.-H. Lin, and C.-T. Lin, "W-band OFDM RoF system with simple envelope detector down-conversion," *Proc. OFC 2015*, Los Angeles, California, W4G. 6.
76. S. Mikroulis, M. P. Thakur, and J. E. Mitchell, "Investigation of a robust remote heterodyne envelope detector scheme for cost-efficient E-PON / 60 GHz wireless integration," *2014 16th International Conference on Transparent Optical Networks (ICTON)*, Graz, pp. 1-4.
77. D. Zibar, R. Sambaraju, A. Caballero, J. Herrera, U. Westergren, A. Walber, J. B. Jensen, J. Marti, and I. Tafur Monroy, "High-capacity wireless signal generation and demodulation in 75- to 110-GHz band employing all-optical OFDM," *IEEE Photon. Technol. Lett.*, vol. 23, no. 12, pp. 810-812, 2011.
78. X. Li, J. Yu, N. Chi, and J. Xiao, "Antenna polarization diversity for high-speed polarization multiplexing wireless signal delivery at W-band," *Opt. Lett.*, vol. 39, no. 5, pp. 1169-1172, 2014.
79. J. Xiao, J. Yu, X. Li, Y. Xu, Z. Zhang, and L. Chen, "20-Gb/s PDM-QPSK signal delivery over 1.7-km wireless distance at W-band," *Proc. OFC 2015,* Los Angeles, California, W4G.4.
80. S. Inudo, Y. Yoshida, A. Kanno, P. Tien Dat, T. Kawanishi, and K.-i. Kitayama, "On the MIMO channel rank deficiency in W-band MIMO RoF transmissions," *Proc. OFC 2015,* Los Angeles, California, W4G. 5.
81. X. Li, J. Yu, N. Chi, and J. Zhang, "Optical-wireless-optical full link for polarization multiplexing quadrature amplitude/phase modulation signal transmission," *Opt. Lett.*, vol. 38, no. 22, pp. 4712-4715, 2013.
82. C. Tang, X. Li, F. Li, J. Zhang, and J. Xiao, "A 30 Gb/s full-duplex bi-directional transmission optical wireless-over fiber integration system at W-band," *Proc. OFC 2014*, San Francisco, California, W2A.4.
83. X. Zhou and J. Yu, "Multi-level, multi-dimensional coding for high-speed and high-spectral-efficiency optical transmission," *J. Lightw. Technol.*, vol. 27, no. 16, pp. 3641-3653, 2009.
84. K. Kikuchi, "Electronic post-compensation for nonlinear phase fluctuations in a 1000-km 20-Gbit/s optical quadrature phase-shift keying transmission system using the digital coherent receiver," *Opt. Express*, vol. 16, no. 2, pp. 889-896, 2008.
85. J. Zhang, X. Li, and Z. Dong, "Digital nonlinear compensation based on the modified logarithmic step size," *J. Lightw. Technol.*, vol. 31, no. 22, pp. 3546-3555, Nov. 2013.
86. E. Ip and J. M. Kahn, "Feedforward carrier recovery for coherent optical communications," *J. Lightw. Technol.*, vol. 25, no. 9, pp. 2675-2692, Sep. 2007.
87. J. Li, E. Tipsuwannakul, T. Eriksson, M. Karlsson and P. A. Andrekson, "Approaching Nyquist limit in WDM systems by low-complexity receiver-side duobinary shaping," *J. Lightw. Technol.*, vol. 30, no. 11, pp. 1664-1676, 2012.
88. K. Koizumi et al., "512 QAM transmission over 240 km using frequency-domain equalization in a digital coherent receiver," *Opt. Express*, vol. 20, no. 21, pp. 23383-23389, 2012.
89. D. Godard, "Passband timing recovery in an all-digital modem receiver," *IEEE Trans. on Commun.*, vol. 26, no. 5, pp. 517-523, 1978.
90. K. Mueller, and M. Muller, "Timing recovery in digital synchronous data receivers," *IEEE Trans. on Commun.*, vol. 24, no. 5, pp. 516-531, 1976.
91. D. Godard, "Self-recovering equalization and carrier tracking in two-dimensional data communication systems," *IEEE Trans. on Commun.*, vol. 28, no. 11, pp. 1867-1875, 1980.
92. F. Gardner, "A BPSK/QPSK timing-error detector for sampled receivers," *IEEE Trans. on Commun.*, vol. 34, no. 5, pp. 423-429, 1986.
93. A. Nafta, P. Johannisson, and M. Shtaif, "Blind equalization in optical communications using independent component analysis," *J. Lightw. Technol.*, vol. 31, no. 12, pp. 2043-2049, 2013.
94. S. Savory, "Digital filters for coherent optical receivers," *Opt. Express*, vol. 16, no. 2, pp. 804-817, 2008.
95. P. Winzer, "High-spectral-efficiency optical modulation formats," *J. Lightw. Technol.,* vol. 30, no. 24, pp. 3824-3835, 2012.
96. A. J. Viterbi, "Error bounds for convolutional codes and an asymtotically optimum decoding algorithm," *IEEE Trans. Inform. Theory*, vol. 13, no. 2, pp. 260-269, Apr. 1967.
97. H.-C. Chien, J. Yu, Z. Jia, Z. Dong and X. Xiao, "Performance assessment of noise-suppressed Nyquist-WDM for Terabit superchannel transmission," J. Lightw. Technol., vol. 30, no. 24, pp. 3965-3971, 2012.
98. T. Pfau, S. Hoffmann, and R. Noe, "Hardware-efficient coherent digital receiver concept with feedforward carrier recovery for M-QAM constellations," *J. Lightw. Technol.*, vol. 27, no. 8, pp. 989-999, Apr. 2009.
99. X. Zhou, "An improved feed-forward carrier recovery algorithm for coherent receivers with M-QAM modulation format," *IEEE Photon. Technol. Lett.*, vol. 22, no. 14, pp. 1051–1053, 2010.
100. I. Fatadin, D. Ives, and S. J. Savory, "Blind equalization and carrier phase recovery in a 16-QAM optical coherent system," *J. Lightw. Technol.*, vol. 27, no. 15, pp. 3042-3049, Aug. 2009.
101. K. Zhong, J. Ke, Y. Gao, and J. Cartledge, "Linewidth-tolerant and low-complexity two-stage carrier phase estimation based on modified QPSK partitioning for dual-polarization 16-QAM systems," *J. Lightw. Technol.,* vol. 31, no. 1, pp. 50-57, 2013.
102. X. Zhou, C. Lu, A. P. T. Lau and K. Long, "Low-complexity carrier phase recovery for square M-QAM based on S-BPS algorithm," *IEEE Photon. Technol. Lett.*, vol. 26, no. 18, pp. 1863-1866, 2014.
103. C. Pan and F. R. Kschischang, "Probabilistic 16-QAM shaping in WDM systems," *J. Lightw. Technol.*, vol. 34, no. 18, pp. 4285-4292, 2016.
104. F. Buchali, F. Steiner, G. Böcherer, L. Schmalen, P. Schulte, and W. Idler, "Rate adaptation and reach increase by probabilistically shaped 64-QAM: An experimental demonstration," *J. Lightw. Technol.,* vol. 34, no. 7, pp. 1599-1609, 2016.
105. Y. Zhu et al., "Spectrally-efficient single-carrier 400G transmission enabled by probabilistic shaping," *Proc. OFC 2017*, Los Angeles, California, M3C.1.
106. J. Yu, J. Zhang, K. Wang, B. Zhu, S. Dzioba, H. Chien, X. Li, Y. Cai, X. Xiao, and J. Shi, "8×506-Gb/s 16QAM WDM signal coherent transmission over 6000-km enabled by PS and HB-CDM," *Proc. OFC 2018*, San Diego, California, M2C.3.
107. K. Wang, X. Li, M. Kong, P. Gou, W. Zhou, and J. Yu, "Probabilistically shaped 16QAM signal transmission in a photonics-aided wireless Terahertz-wave system," *Proc. OFC 2018*, San Diego, California, M4J.7.
108. X. Li, J. Yu, L. Zhao, K. Wang, W. Zhou, and J. Xiao, "1-Tb/s photonics-aided vector millimeter-wave signal wireless delivery at D-band," *Proc. OFC 2018*, San Diego, California, Th4D.1.
109. X. Li, J. Yu,, L. Zhao, K. Wang, C. Wang, M. Zhao, W. Zhou, and J. Xiao, "1-Tb/s millimeter-wave signal wireless delivery at D-band," *IEEE/OSA J. Lightw. Technol.,* vol. 37, no. 1, pp. 196-204, 2019.
110. Recommendation I T U. Attenuation by atmospheric gases. ITU-R P. 676, 2009.
111. Y. Xu, Z. Zhang, J. Xiao, and J. Yu, "W-band millimeter wave communication," *Journal of Terahertz Science and Electronic Information Technology*, vol. 12, no. 4, pp. 554-558, 2014.
112. J. Xiao, J. Yu, X. Li, Y. Xu, Z. Zhang, and L. Chen, "40-Gb/s PDM-QPSK signal transmission over 160-m wireless distance at W-band," *Opt. Lett.,* vol. 40, pp. 998-1001, 2015.
113. X. Li and J. Yu, "Photonics-aided 32-Gb/s wireless signal transmission Over 1 km at K-band," *IEEE Photon. Technol. Lett.,* vol. 29, no. 13, pp. 1120-1123, 2017.
114. J. Yu, "Photonics-assisted millimeter-wave wireless communication," *IEEE J. of Quantum Electron.*, vol. 53, pp. 1-17, 2017.
115. J. Yu, X. Li, J. Zhang, and J. Xiao, "432-Gb/s PDM-16QAM signal wireless delivery at W-band using optical and antenna polarization multiplexing," *Proc. ECOC 2014*, Cannes, France, We.3.6.6.